

An Unbiased CO Survey Toward the Northern Region of the Small Magellanic Cloud with the Atacama Compact Array. I. Overview: CO Cloud Distributions

KAZUKI TOKUDA,^{1,2} HIROSHI KONDO,¹ TAKAHIRO OHNO,³ AYU KONISHI,¹ HIDETOSHI SANO,² KISETSU TSUGE,³ SAROLTA ZAHORECZ,^{1,2} NAO GOTO,¹ NASLIM NEELAMKODAN,⁴ TONY WONG,⁵ MARTA SEWILO,^{6,7} HAJIME FUKUSHIMA,⁸ TATSUYA TAKEKOSHI,⁹ KAZUYUKI MURAOKA,¹ AKIKO KAWAMURA,² KENGO TACHIHARA,³ YASUO FUKUI,³ AND TOSHIKAZU ONISHI¹

¹*Department of Physical Science, Graduate School of Science, Osaka Prefecture University, 1-1 Gakuen-cho, Naka-ku, Sakai, Osaka 599-8531, Japan*

²*National Astronomical Observatory of Japan, National Institutes of Natural Science, 2-21-1 Osawa, Mitaka, Tokyo 181-8588, Japan*

³*Department of Physics, Nagoya University, Chikusa-ku, Nagoya 464-8602, Japan*

⁴*Department of physics, United Arab Emirates University, Al-Ain, 15551, UAE*

⁵*Department of Astronomy, University of Illinois, Urbana, IL 61801, USA*

⁶*CRESST II and Exoplanets and Stellar Astrophysics Laboratory, NASA Goddard Space Flight Center, Greenbelt, MD 20771, USA*

⁷*Department of Astronomy, University of Maryland, College Park, MD 20742, USA*

⁸*Center for Computational Sciences, University of Tsukuba, Ten-nodai, 1-1-1 Tsukuba, Ibaraki 305-8577, Japan*

⁹*Kitami Institute of Technology, 165 Koen-cho, Kitami, Hokkaido 090-8507, Japan*

(Received; Revised; Accepted)

Submitted to ApJ

ABSTRACT

We have analyzed the data from a large-scale CO survey toward the northern region of the Small Magellanic Cloud (SMC) obtained with the Atacama Compact Array (ACA) stand-alone mode of ALMA. The primary aim of this study is to comprehensively understand the behavior of CO as an H₂ tracer in a low-metallicity environment ($Z \sim 0.2 Z_{\odot}$). The total number of mosaic fields is ~ 8000 , which results in a field coverage of 0.26 degree^2 ($\sim 2.9 \times 10^5 \text{ pc}^2$), corresponding to $\sim 10\%$ area of the galaxy. The sensitive $\sim 2 \text{ pc}$ resolution observations reveal the detailed structure of the molecular clouds previously detected in the single-dish NANTEN survey. We have detected a number of compact CO clouds within lower H₂ column density ($\sim 10^{20} \text{ cm}^{-2}$) regions whose angular scale is similar to the ACA beam size. Most of the clouds in this survey also show peak brightness temperature as low as $< 1 \text{ K}$, which for optically thick CO emission implies an emission size much smaller than the beam size, leading to beam dilution. The comparison between an available estimation of the total molecular material traced by thermal dust emission and the present CO survey demonstrates that more than $\sim 90\%$ H₂ gas cannot be traced by the low- J CO emission. Our processed data cubes and 2-D images are publicly available.

Keywords: stars: formation — ISM: clouds — ISM: — galaxies: Local Group

1. INTRODUCTION

During the lifecycle of the interstellar medium, galaxy evolution is characterized by increasing abundance of heavy elements that are heavier than H and He, i.e., metallicity, as a consequence of star formation. The metallicity has a large impact on the cooling/heating process from interstellar gas, which results in regulating star formation therein. Observational studies toward star-forming regions in the solar neighborhood alone cannot explore a wide range of the

parameter space, and extragalactic star-forming regions are thus vital targets, especially to investigate low-metallicity environments.

The Large Magellanic Cloud ($D \sim 50$ kpc, [de Grijs et al. 2014](#)) and the Small Magellanic Cloud ($D \sim 62$ kpc, [Graczyk et al. 2020](#)) are the nearest galaxies to investigate the star formation in such an environment. Their proximity enables us to obtain high spatial resolution views resolving individual star-forming regions, such as molecular cloud cores and individual protostar or protostellar systems. The metallicity of the SMC is $Z \sim 0.2 Z_{\odot}$ ([Russell & Dopita 1992](#); [Rolleston et al. 1999](#); [Pagel 2003](#)), which is a sufficiently sub-solar regime and lower than that of the LMC ($Z \sim 0.5 Z_{\odot}$, [Rolleston et al. 2002](#)). The low-metal condition is approximate to the most active phase of star formation during cosmic history ([Pei et al. 1999](#)). It has therefore been the target of a large number of comprehensive surveys in multiple wavelengths aiming at a better understanding of the behavior of interstellar gas and young stellar objects (YSOs). The previous millimeter observations with small aperture telescopes, CfA 1.2m and NANTEN, revealed the overall distribution of the high-density molecular gas traced by CO ([Rubio et al. 1991](#); [Mizuno et al. 2001](#)) in the SMC at spatial resolutions of 150 or 45 pc. Spitzer/Herschel observations provided a high-dynamic-range view of cold/warm gas ([Bolatto et al. 2007, 2011](#); [Gordon et al. 2011, 2014](#); [Jameson et al. 2016](#)) as well as the young stellar population (e.g., [Oliveira et al. 2013](#); [Sewilo et al. 2013](#); [Ruffle et al. 2015](#)). Ground-based observations detected millimeter/submillimeter dust continuum emission from not only bright CO clouds ([Bot et al. 2010](#); [Hony et al. 2015](#); [Takekoshi et al. 2017, 2018](#)) but also fainter clouds, which are likely to be cold molecular material that was not accessible with the previous CO surveys ([Takekoshi et al. 2017](#)). The newly developed Australian Square Kilometre Array Pathfinder (ASKAP) interferometer has been updating the atomic hydrogen (H I) view in the SMC. The pilot study by [McClure-Griffiths et al. \(2018\)](#) reported outflowing gas, and the excellent data set is also useful to search for some indications of the last interaction between this galaxy and the LMC based on the detailed velocity field ([Murray et al. 2019](#)).

Among these surveys, the angular resolution of CO surveys was especially not high enough to investigate the detailed structures which are directly related to the star formation activities therein. Larger aperture single-dish telescopes performed ~ 10 pc resolution observations in CO but covered only small fields in the galaxy ([Rubio et al. 1993](#); [Bolatto et al. 2003](#); [Muller et al. 2010](#)). In addition to the coarse resolution, sensitivity, and field coverage of the previous studies, CO observations intrinsically have a particular problem as a molecular gas tracer, especially in a low-metallicity environment. Theoretical modeling demonstrates that UV photons penetrate more deeply into dust-poor molecular clouds, and thus a large portion of molecular clouds become ‘‘CO dark’’ (e.g., [Glover & Clark 2012](#); [Fukushima et al. 2020](#); [Bisbas et al. 2021](#)). In such an extreme condition, some theoretical works ([Glover & Clark 2016](#)) and observations of distant galaxies claimed that [C I] more efficiently probes H_2 clouds than CO ([Papadopoulos et al. 2004](#); [Alaghband-Zadeh et al. 2013](#)). However, [Okada et al. \(2015, 2019\)](#) reported that both CO and [C I] emission show similar distributions in some of the molecular clouds in the LMC. In any case, observation efficiencies with current instruments at the high-frequency (492 GHz for [C I]) band is not high enough to obtain comprehensive maps across galaxies in the Local Group. According to [Requena-Torres et al. \(2016\)](#), [C II] emission does not have significant contributions from atomic and ionized hydrogen gas and works as a better tracer of the total H_2 mass/column density toward their observed regions in the SMC. Nevertheless, faint CO emission enables us to trace H I– H_2 transition layers and overall H_2 structures seen in [C II] ([Jameson et al. 2018](#)). The low/mid- J CO transitions in lower frequency bands are suitable for faster observations covering a large field thanks to the atmospheric condition and the larger beam size of the telescopes. Thus, despite its limitations, low- J CO mapping remains the clearest guide to the distribution of molecular gas if sufficient sensitivity and resolution can be achieved.

Recent ALMA CO and its isotopologue observations have been revealing detailed molecular cloud distributions in the Local Group galaxies, the LMC and M33 (e.g., [Indebetouw et al. 2013](#); [Wong et al. 2017](#); [Naslim et al. 2018](#); [Tokuda et al. 2020a](#); [Muraoka et al. 2020](#); [Kondo et al. 2021](#)). These studies demonstrated that \lesssim a few pc resolution observations are powerful to distinguish the different properties among the observed Giant Molecular Clouds (GMCs) depending on their evolutionary stages ([Sawada et al. 2018](#); [Wong et al. 2019](#)) and to find indications of cloud interactions initiating high-mass star formation ([Fukui et al. 2015a, 2019](#); [Saigo et al. 2017](#); [Tokuda et al. 2019](#); [Sano et al. 2021](#)). Although the total number of ALMA CO studies in the SMC is limited, recent observations have been revealing the density structure of molecular clouds ([Muraoka et al. 2017](#); [Jameson et al. 2018](#); [Neelamkodan et al. 2021](#)).

To reveal CO distributions in the SMC comprehensively, we need high-angular resolution data with wide spatial coverage. Use of the Atacama Compact Array (ACA, a.k.a. Morita Array) stand-alone mode is an ideal option to perform an unbiased large-scale survey as demonstrated by a dense core study in Taurus ([Tokuda et al. 2020b](#)). Some CO survey programs covering a square degree scale are also ongoing in the SMC (e.g., #2018.1.01115.S, [Jameson et al.](#)

in prep). At the CO($J = 2-1$) frequency (230 GHz), the ACA observations provide a beam size of $\sim 6''$ corresponding to ~ 2 pc at the distance of ~ 62 kpc (Graczyk et al. 2020). In this study, we investigated a Northern region in the SMC. One of the advantages of this region is that the velocity components in H I are relatively simple compared to the more CO bright South-West (SW) region (c.f., Stanimirović et al. 1999; McClure-Griffiths et al. 2018). On the other hand, the Northern region contains several H II regions, including the brightest one (N66, Massey et al. 1989) in the SMC, and a few well-studied supernova remnants (SNRs), SNR B0102-72.3 (e.g., Badenes et al. 2010; Maggi et al. 2019) and SNR B0057-72.2 (e.g., Ye et al. 1991; Nazé et al. 2002). The presence of various evolutionary stages of the interstellar medium allows us to explore the behavior of CO in various environments of this low-metallicity galaxy.

We present ALMA-ACA archival CO data toward the Northern region in this paper. The data set is quite large, and thus we mostly focus on an overall description of the CO emission properties. Sect. 2 describes the observations and data reduction, and then we show the fundamental CO and continuum maps in Sect. 3. Sect. 4 gives some early analysis characterizing the CO clouds and discusses their properties.

2. OBSERVATIONS AND DATA REDUCTION

We retrieved the data from the ALMA Observatory Project 2017.A.00054.S, one of the six filler programs¹ for the ACA stand-alone observations in Cycle 5/6. The main target lines were CO($J = 2-1$) in Band 6 (~ 230 GHz) and CO($J = 1-0$) in Band 3 (~ 115 GHz). The total number of mosaic fields for the Band 6 and Band 3 programs were 7749 and 1939, respectively, with the ACA 7 m array stand-alone mode. The resultant field coverage in both bands is ~ 0.26 degree², which is one of the largest observing fields among ALMA studies in Local Group galaxies. Figure 1 represents the observed field in Band 6+3 on the entire H α map in the SMC. The frequency resolution and the total bandwidth in Band 6 were 122 kHz and 250 MHz, respectively. For Band 3, the total bandwidth is the same, while the frequency resolution is two times better than that in Band 6 to match the velocity resolution of both bands at ~ 0.16 km s⁻¹. The central frequencies of the individual continuum setting were [112.5, 102.4, 100.2] GHz for Band 3, and [229.0, 215.3, 213.3] GHz for Band 6 with a 2 GHz bandwidth in each window. The aggregate bandwidth for the continuum data integrating all of the available spectral windows was 6 GHz. The TP (Total Power) array observations

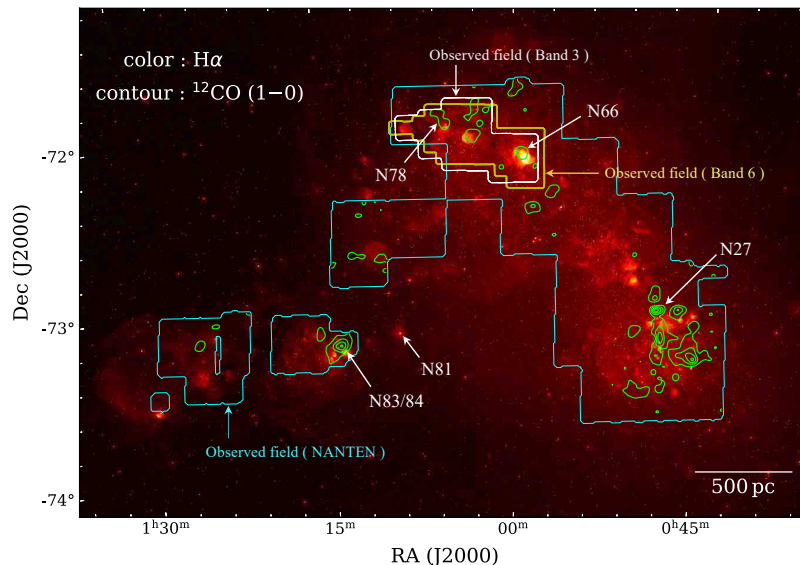


Figure 1. Observed fields with the ACA stand-alone mode on an H α map (Smith & MCELS Team 1999) in the SMC. The yellow and white lines show the regions of Band 6 and Band 3 observations, respectively. The cyan lines denote the observed field boundaries with the NANTEN survey and green contours represent the CO($J = 1-0$) map (Mizuno et al. 2001; see also Fukui & Kawamura 2010). The lowest contour level and contour steps are 0.3 K km s⁻¹ and 0.6 K km s⁻¹, respectively. Note that the NANTEN field coverage was extended from the publication of the first survey paper (the NANTEN team, Fukui et al. private communication).

¹ <https://almascience.nao.ac.jp/news/alma-announces-aca-observatory-filler-programs-for-cycle-6>

in Band 6 were performed to supplement spatially extended emission with the same frequency setting. The beam size and sensitivity of the TP array observations are $30''6$ and ~ 0.04 K at the native velocity resolution.

We used the Common Astronomy Software Application (CASA) package (McMullin et al. 2007) version 5.4.0 in the data reduction. We did not change the calibration scheme provided by the ALMA observatory while we performed the imaging process after concatenating all visibility files, which are separately provided in the archive. Although the beam shapes, i.e., sizes of the major and minor axes, of the individual observing tiles differ slightly, the aspect ratio distribution ranges 1.1-1.9 with a median value of 1.1. The final beam shape of the connected data was automatically determined by the `tclean` procedure using `restoringbeam = "common"` with the natural weighting. The `multi-scale` deconvolver (Kepley et al. 2020) was used to recover extended emission as much as possible. The imaging grid of Band 6 and Band 3 were set to have square pixels of $2''0$ and $4''0$, respectively, and the scales of the `multi-scale` were 0, 3, and 9 pixels, which roughly corresponds to 0, 1, and 3 times of the beam size. With the `auto-multithresh` technique, we select the emission mask in the dirty and residual image. The parameters were follows; `sidelobethreshold = 1.25`, `noisethreshold = 3.0`, `lownoisethreshold = 1.5`, `smoothfactor = 1.2`, and `minbeamfrac = 0.05`. We continued the deconvolution process until the peak intensity of the residual image reached the $\sim 1\sigma$ noise level. We made continuum image in the same manner except for the emission mask selection scheme of the `tclean`. We manually selected the emission mask in the continuum images because we could find only one or two significant sources (see Sect. 3.2 and Figures 9 and 10 in Appendix A).

To estimate the missing flux of the Band 6 7 m array data in $\text{CO}(J = 2-1)$, we made a spatially smoothed 7 m array data cube and then compared the flux with the TP array alone. The resultant missing flux varies from region to region (see Figure 11 in Appendix A), but more than half of the total flux is captured by the 7 m array alone, whose maximum recovered scale is $\sim 30''$, corresponding to ~ 9 pc. Nevertheless, we combined the 7 m and TP array data using the `feather` task to compensate for the extended emission. We used the combined $\text{CO}(J = 2-1)$ data throughout this study. Table 1 summarizes the final beam size and the typical r.m.s sensitivity in each data. The angular resolution and sensitivity of the $\text{CO}(J = 2-1)$ data are better than the 1-0 data, and we mainly present the former one throughout this paper. The 1.3 mm and 2.6 mm continuum data are used to identify dense materials around massive protostellar sources (Sect. 3.2 and Appendix A), and the $\text{CO}(J = 1-0)$ maps are mainly presented in Appendix B.

To minimize the noise contribution, we made a moment-masked cube data (e.g., Dame 2011) when we obtain moment 0, 1 and 2 maps (see Sect 3.1). Based on a velocity/spatially smoothed data cube, we determined the emission-free pixels, which are less than $\sim 3\sigma$ level, and set them to zero value. An additional criterion for creating emission masks is whether the CO emitting regions more than $\sim 3\sigma$ are continuously connected to each other over 20 voxels, and thus very tiny features whose size is smaller than the resolution elements are ignored. However, The fraction of the real emissions that were not selected as positive masks is not large because the masked moment maps fairly reproduce the overall distributions of the peak temperature map, which is made of the unmasked cube data (see Figures 2 and 3 in Sect. 3.1.)

Table 1. Summary of the processed data quality

Data	Beam size	Velocity resolution (km s^{-1})	r.m.s (K)	r.m.s (Jy beam^{-1})
$\text{CO}(J = 2-1)$	$6''9 \times 6''6$	0.5	~ 0.06	$\sim 9 \times 10^{-2}$
$\text{CO}(J = 1-0)$	$14''9 \times 11''3$	0.5	~ 0.22	$\sim 4 \times 10^{-1}$
1.3 mm continuum	$7''2 \times 6''7$	$\sim 2 \times 10^{-3}$
2.6 mm continuum	$15''8 \times 12''6$	$\sim 2 \times 10^{-3}$

The final reduced fits images, CO cubes and continuum 2-D maps, are available at [10.5281/zenodo.4628967](https://doi.org/10.5281/zenodo.4628967).

3. RESULTS

3.1. Overall Distribution of $\text{CO}(J = 2-1)$ clouds in the SMC North region

Figure 2 shows the integrated intensity $\text{CO}(J = 2-1)$ map toward the SMC North region. For the first time, the ACA observations have revealed the presence/absence of CO clouds and their distributions in this particular part of the galaxy with a high spatial dynamic range whose size scale is from ~ 2 pc to more than ~ 1 kpc. As shown in panel (a,b), the relatively bright/large CO clouds are distributed in and around the H II regions (LHA 115-N N66 (N66),

LHA 115-N N78 (N78), and LHA 115-N N80 (N80), [Henize 1956](#)) and SNRs (B0102-72.3, B0057-72.2). The locations of these clouds on the Herschel map (Panel (b)) are close to the local peaks of the continuum emission. Although these clouds are mostly detected by the previous NANTEN survey ([Mizuno et al. 2001](#)), we successfully detected much smaller/faint clouds, whose size scale is a few parsecs across the observed field, around the large clouds. These clouds are real emission instead of noise-like features (see also some examples shown in Sect. 4.2.1). They do not necessarily correlate with the local peak of the Herschel dust emission and the minimum intensity of $250\mu\text{m}$ emission with CO emission is $\sim 5\text{MJy sr}^{-1}$. In Sect. 4.2, we further discuss how CO emission traces molecular clouds in this galaxy.

Figure 3 (a) represents the CO peak brightness temperature (T_{peak}) map. The typical temperature is a few kelvins throughout the observed field, which is remarkably weaker than 10 K, although similar spatial resolution studies in the MW (Milky Way) and M33 show more bright emission greater than 10K. One of the possible interpretations to explain the faint nature of CO emission is the beam dilution effect. The CO clouds are too small to spatially resolve even with the $\sim 2\text{pc}$ resolution (see more detailed discussion in Sect. 4.2). The moment 1 map in panel (b) shows the velocity distribution in CO. The dominant velocity components in this region are $\sim 160\text{--}170\text{ km s}^{-1}$. Some clouds show velocity gradient across their minor/major elongations; the others show more complex velocity fields. We found a remarkable difference: the N78 region is $\sim 10\text{--}20\text{ km s}^{-1}$ redshifted compared to the average velocity. Panel (b) illustrates the moment 2 map with a displayed range of $0\text{--}5\text{ km s}^{-1}$. The large clouds (see the previous paragraph) tend to show larger velocity dispersion, $\sim 2\text{--}3\text{ km s}^{-1}$, around their CO peak in the moment 1 or T_{peak} maps.

Figure 4 illustrates the velocity-channel map with the Herschel $250\mu\text{m}$ contours as reference positions. Most of the bright dust emitting regions are visible in CO (see also Figure 2). The representative velocity of the N66, SNR B0102-72.3, N78, and N80 regions are 160, 168, 184, 160 km s^{-1} , respectively.

3.2. Millimeter continuum sources in the N78 region

We detected significant ($>3\sigma$) continuum emission only around CO intense positions in the N78 region. Figure 5 shows a zoomed-in view of the CO($J = 2\text{--}1$) and continuum maps. We detected at least two continuum sources in 1.3 mm (see panel(b)): the measured fluxes of the northern (MMS-1) and southern (MMS-2) sources are $\sim 230\text{ mJy}$ and $\sim 130\text{ mJy}$, respectively. MMS-1 is bright in 2.6 mm also (panel (c)), whose flux is $\sim 160\text{ mJy}$. The spectral index derived from the two bands in the northern source is ~ 0.5 , indicating that the continuum flux in MMS-1 is likely dominated by the free-free emission rather than thermal dust emission.

We found YSO (candidate) associations to the two millimeter sources based on the [Sewilo et al. \(2013\)](#) catalog. The source in MMS-2 is the most luminous source ($L \sim 1.5 \times 10^5 L_{\odot}$) within the ACA field. The estimated stellar mass is $\sim 28 M_{\odot}$. [Oliveira et al. \(2013\)](#) confirmed that it is indeed a YSO (#28) using their spectroscopic observations. The millimeter continuum emission is useful to probe the presence of massive/dense clumps around a massive protostar. The total 1.3 mm flux of MMS-2 infers that the gas mass is $\sim 6 \times 10^3 M_{\odot}$ assuming the gas-to-dust ratio of 1000 (e.g., [Roman-Duval et al. 2014](#)), dust opacity of $1\text{ cm}^{-2}\text{ g}^{-1}$ (e.g., [Ossenkopf & Henning 1994](#)), and dust temperature of 24 K ([Takekoshi et al. 2018](#)).

4. DISCUSSION

4.1. Mass Estimation of CO clouds and the Detection Limit of the Survey

There is no unique way to estimate molecular cloud mass based on the CO observation, mostly due to the uncertainty in the CO($J = 1\text{--}0$)-to- H_2 conversion (X_{CO}) factor (see the review by [Bolatto et al. 2013](#)) and intensity ratios of CO($J = 2\text{--}1$) and CO($J = 1\text{--}0$) (hereafter, $R_{2\text{--}1/1\text{--}0}$) throughout the galaxy. Nevertheless, we tentatively estimate the mass detection limit based on the survey sensitivity and resolution elements. The 1σ noise level of the data cube of $\sim 0.06\text{ K}$ and the typical line width of the CO clouds of 1.5 km s^{-1} make that the 1σ noise level of the integrated intensity is $\sim 0.05\text{ K km s}^{-1}$. We tentatively set the detection criteria as that the CO emission region is larger than the single beam element ($\sim 2\text{ pc}$) at more than 3σ , and the detection limit in the CO luminosity itself is $\sim 1.0\text{ K km s}^{-1}\text{ pc}^2$.

[Bolatto et al. \(2003\)](#) performed CO($J = 2\text{--}1$) and CO($J = 1\text{--}0$) observations toward the SMC N83/N84 clouds with SEST and derived average $R_{2\text{--}1/1\text{--}0}$ as ~ 0.9 . Although the sensitivity is not high enough to derive $R_{2\text{--}1/1\text{--}0}$ at the native resolution of CO($J = 1\text{--}0$), we obtained a similar result, $R_{2\text{--}1/1\text{--}0} \sim 1$ (see Appendix B). These values are remarkably higher than those in the MW average, ~ 0.6 ([Yoda et al. 2010](#)), and the other CO bright nearby galaxies, which are $0.6\text{--}0.8$ ([Yajima et al. 2021](#)). In the typical MW molecular clouds, the $J = 2\text{--}1$ line is not fully thermalized and $R_{2\text{--}1/1\text{--}0}$ does not approach to 1 ([Sakamoto et al. 1994](#); [Yoda et al. 2010](#); [Nishimura et al. 2015](#)). One possible explanation of this discrepancy is that the SMC CO observations trace a much deeper side of molecular clouds whose

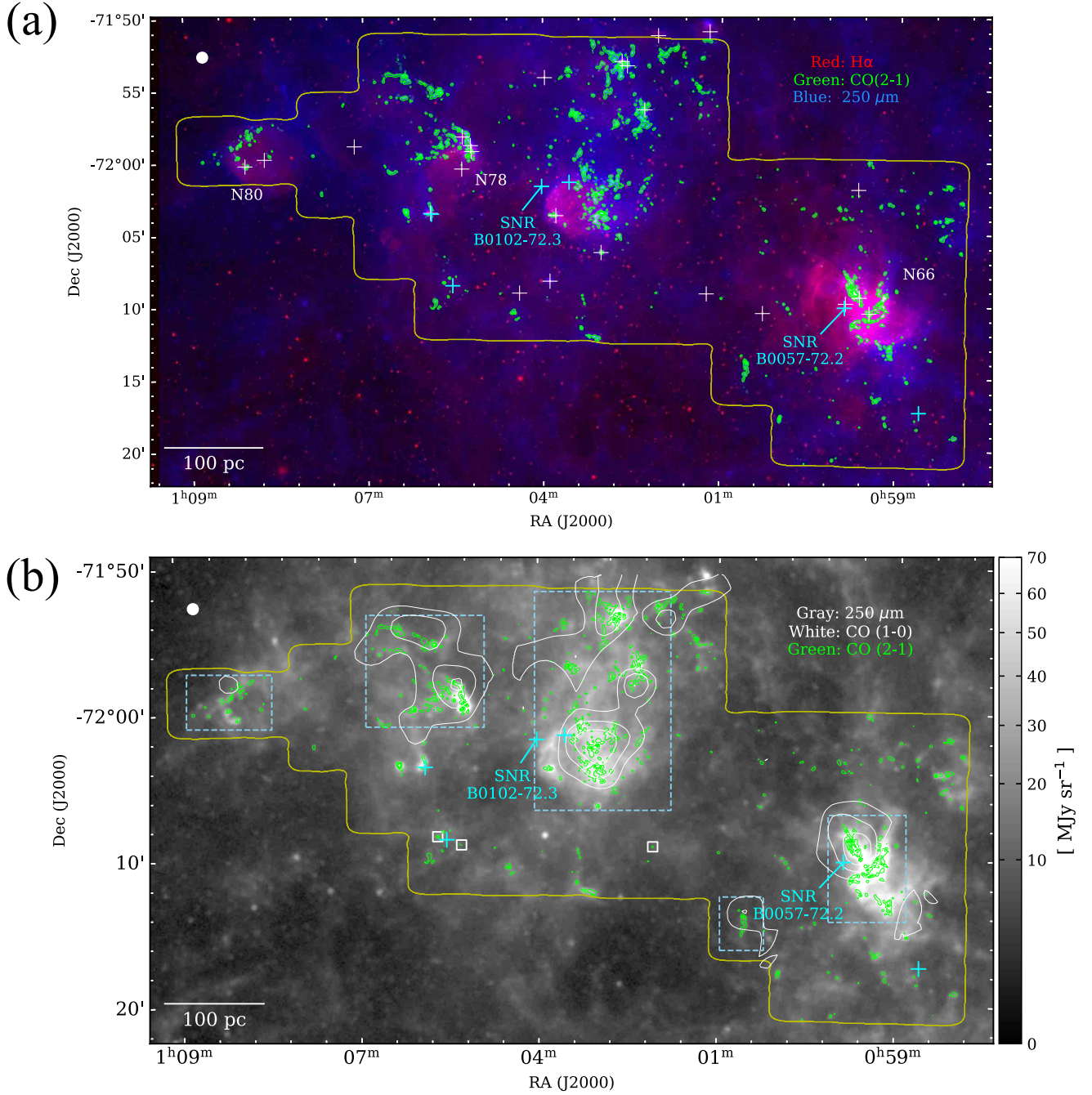


Figure 2. The integrated intensity (moment 0) map of CO($J = 2-1$) toward the SMC North region obtained by the ACA stand-alone mode. (a) The three-color composite image combining the ACA integrated intensity (moment 0) CO($J = 2-1$) (green) $\text{H}\alpha$ (red) (Smith & MCELS Team 1999), and Herschel/SPIRE $250\ \mu\text{m}$ (Gordon et al. 2014) maps. The green contours correspond to the CO($J = 2-1$) emission with contour levels of [1, 6, 11, 16] K km s^{-1} . The yellow line denotes the field coverage of the ACA observations. The circle in the upper-left corner shows the size of the single mosaicing field with the ACA. The white and cyan crosses represent positions of H II regions (Henize 1956) and SNRs (Maggi et al. 2019), respectively. (b) Same as (a) but for the Herschel/SPIRE $250\ \mu\text{m}$ map in gray-scale. The white contours show the NANTEN CO($J = 1-0$) map. The area enclosed by the cyan dashed rectangles roughly represent the regions with the known CO clouds detected by the NANTEN survey (see also the text in Sect. 4.2.1). The three small squares represent the examples of compact CO clouds shown in Figure 6 (see Sect. 4.2.1).

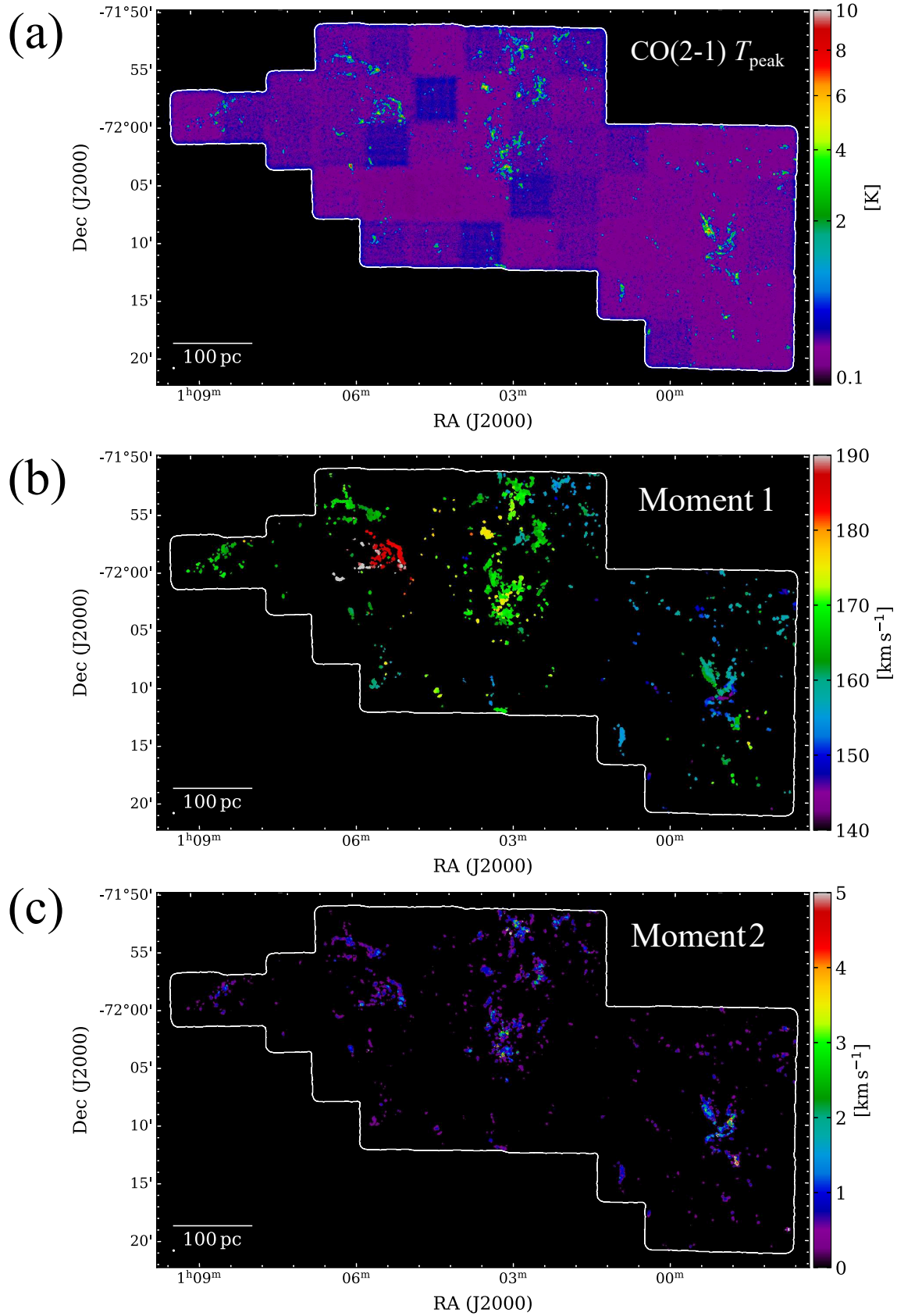


Figure 3. Panel (a), (b), and (c) show the CO($J = 2-1$) peak brightness temperature, centroid velocity (moment 1), and velocity dispersion (moment 2) maps, respectively.

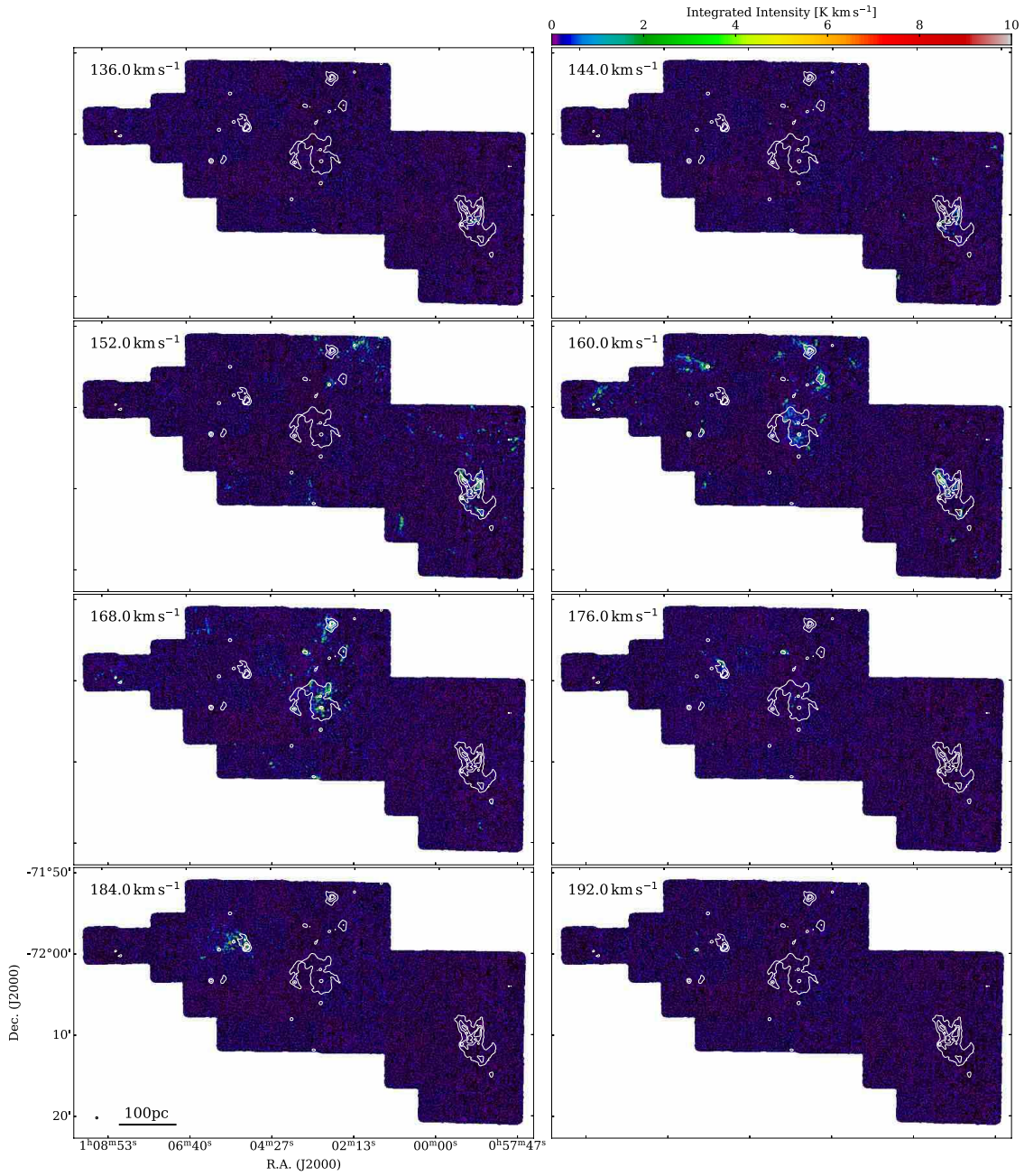


Figure 4. Velocity-channel maps toward the SMC North in CO($J = 2-1$). The lowest velocity is shown in the upper left corner of each panel. The beam size of the ACA CO observations is shown by the black ellipse in the lower-left corner of the lower-left panel. The white contours show the Herschel/SPIRE 250 μm map with the contour levels of [40, 80, 120] MJy sr $^{-1}$.

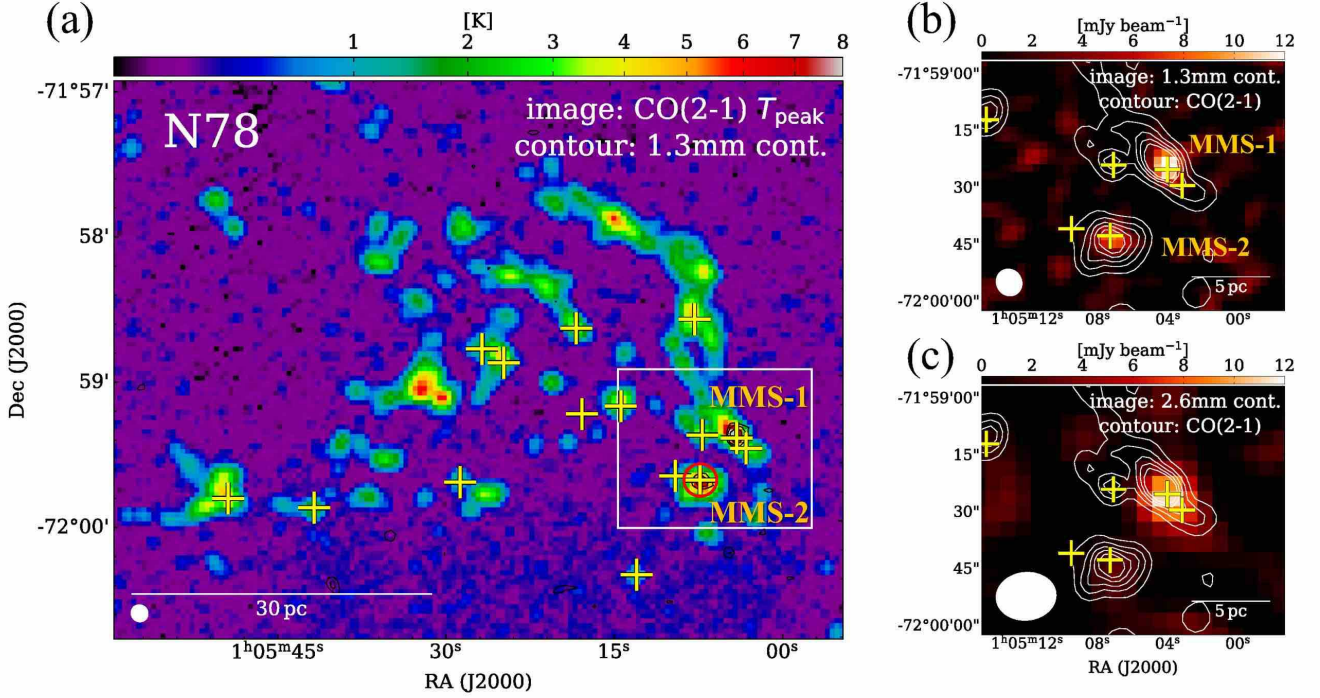


Figure 5. (a) An enlarged view of the CO($J = 2-1$) peak brightness temperature (T_{peak}) map around the N78 region. The black contours show the 1.3 mm continuum image with the contour levels of $[5, 7, 10] \text{ mJy beam}^{-1}$. The white rectangle corresponds to the visualized area in panel (b,c). The white ellipse in the lower-left corner shows the beam size of CO($J = 2-1$). The yellow crosses denote the positions of the YSO candidates (Sewilo et al. 2013). The red circle is a confirmed YSO by the spectroscopic observation (Oliveira et al. 2013). (b) Color-scale and contours represent the 1.3 mm continuum and CO($J = 2-1$) T_{peak} maps, respectively. The lowest CO($J = 2-1$) contour level and contour step are 1.0 K, and 1.0 K, respectively. The white ellipse in the lower-left corner gives the beam size of the continuum image. (c) Same as panel (b) but for the Band 3 (2.6 mm) continuum data.

density is $\sim 10^4 \text{ cm}^{-3}$ (see Muraoka et al. 2017). In this case, densities of CO emitting region are close to or higher than the critical density of $J = 2-1$ line, and $R_{2-1/1-0}$ becomes ~ 1 . Numerical modelings of molecular cloud adopting the SMC-like metallicity also reproduced a similar ratio, possibly due to the proposed reason (c.f., Bisbas et al. 2021), i.e., tracing a higher density region than the MW by the CO observations. Sect. 4.2 further explains the high-density nature of CO clouds in the observed region. In summary, our tentative use of $R_{2-1/1-0}$ as 0.9–1.0 seems to be reasonable based on the available measurements.

Mizuno et al. (2001) estimated the X_{CO} factor in the SMC (hereafter, $X_{\text{CO}}^{\text{SMC}}$) as $2.5 \times 10^{21} \text{ cm}^{-2} (\text{K km s}^{-1})^{-1}$ assuming of the virial equilibrium throughout the observed cloud. Their estimation is an order of magnitude higher than the Milky Way standard value (e.g., Dame et al. 2001; Bolatto et al. 2013), however the larger beam size ($\sim 45 \text{ pc}$) likely makes a large uncertainty of the cloud radii to derive the virial mass. Higher angular resolution CO data with the same analysis estimated $X_{\text{CO}}^{\text{SMC}}$ as $(4-7.5) \times 10^{20} \text{ cm}^{-2} (\text{K km s}^{-1})^{-1}$ (Bolatto et al. 2003; Muraoka et al. 2017). The previous measurements tell us that the conversion factor is a few or several times larger than X_{CO} in the MW. We tentatively use X_{CO} of $\sim 6 \times 10^{20} \text{ cm}^{-2} (\text{K km s}^{-1})^{-1}$ ($= \alpha_{\text{CO}}$ of $13 M_{\odot} (\text{K km s}^{-1} \text{ pc}^2)^{-1}$), which is mean value from the literature (Bolatto et al. 2003; Muraoka et al. 2017), and $R_{2-1/1-0}$ of 0.9 to estimate the mass of the CO clouds in this study. The uncertainty is supposed to be a factor of ~ 2 . In this case, the luminosity detection criteria of $\sim 1.0 \text{ K km s}^{-1} \text{ pc}^2$ can be converted into $\sim 10-20 M_{\odot}$ as the mass detection limit. Note that the current large-data set can be used to estimate the X_{CO} factor as well, but the method is not decoupled from a complex cloud identification scheme. Although we partially applied cloud decomposition analysis toward some of the simple/isolated clouds in the observed field (Sect. 4.2.1), a separate paper will perform further comprehensive analyses to obtain the full cloud catalog, including their individual physical properties and X_{CO} factor.

4.2. CO cloud properties and the behavior of CO as a tracer

4.2.1. Compact CO clouds

The angular resolution and mass detection sensitivity of the NANTEN survey were 45 pc and $10^4 M_{\odot}$, respectively, which allows us to identify GMCs in terms of studies in the MW-like galaxies. Similar angular resolution studies in LMC/M33 and nearby galaxies with large-aperture single dishes (e.g., Fukui et al. 2008; Tosaki et al. 2011; Onodera et al. 2010, 2012; Miura et al. 2012; Corbelli et al. 2017) and interferometers (e.g., Schinnerer et al. 2013; Pety et al. 2013; Sun et al. 2018; Brunetti et al. 2021) discovered more than a few hundred GMCs per galaxies. However, the CO emission in the SMC is remarkably weaker than that in the above galaxies, and thus Mizuno et al. (2001) predicted a clumpy CO distribution within the NANTEN beam. The present ACA survey revealed the NANTEN identified sources are likely molecular cloud clusters rather than an individual GMC, at least in the CO traced view, which is reasonably consistent with the Mizuno et al. (2001) prediction (see also the enlarged and high-resolution view of N66 in Sect. 4.2.2).

There are many isolated/compact clouds outside the NANTEN-detected regions (see the cyan rectangles in Figure 2). After the NANTEN survey (Mizuno et al. 2001), the subsequent follow-up CO studies in the SMC North region (Muller et al. 2010) did not observe the outside regions. Any previous single-dish observations thus could not find such compact entities. We call them “the compact CO clouds” hereafter. The comparison between the CO and Herschel maps tells us that the submillimeter ($250 \mu\text{m}$) continuum emission does not exceed more than 25 Mjy sr^{-1} at the location of the compact CO clouds. This result means that the compact CO clouds are embedded at the lower hydrogen column density regions if we assume the thermal dust emission is approximately proportional to the total hydrogen material.

We characterize the properties of the compact CO clouds. Because most of them are spatially well-separated at the lowest contour level (see Figure 2), identifying the individual components is straightforward compared to more complex NANTEN-detected clouds. We applied the `astrodendro` algorithm (Rosolowsky et al. 2008) to the CO($J=2-1$) moment-masked data cube (see Sect. 2) outside the dashed cyan rectangles in Figure 2(b). There are three input parameters, `min_value`, `min_delta`, and `min_npix` in the algorithm. The first argument is the minimum intensity value to consider in the cube data; we set this value as 0 K to capture weaker emission as much as possible. The second is the threshold value for entities in close proximity to each other to be regarded as independent components; our adapted value is 0.18 K, corresponding to $\sim 3\sigma$ noise level of the cube data. We set `min_npix`, which is the minimum voxel number with significant emission, as 53 that equivalents to the number having at least a single beam element in XY space and three pixels in the velocity direction. We extracted the largest continuous structures, called “trunk”. The resultant boundaries of the identified sources are almost same as the lowest contour level on their moment 0 map (Figure 2). We estimated the physical quantities of the compact CO clouds, peak brightness temperature (T_{peak}), velocity dispersion (σ_v), CO($J=2-1$) luminosity ($L_{\text{CO}(2-1)}$), beam-deconvolved radius (R_{deconv}), H₂ column density (N_{H_2}), total molecular mass (M_{CO}), and average volume density (n_{H_2}).

Table 2 shows the typical (median) physical parameters of the compact CO clouds. The total mass of the other CO clouds inside the cyan rectangles in Figure 2, is calculated to be $\sim 3.2 \times 10^5 M_{\odot}$. The mass fraction of the compact CO clouds is $\sim 20\%$ with respect to the total mass within the observed field. Since the previous NANTEN survey with a 45 pc resolution was not able to detect such compact emission, these high sensitivity/angular resolution observations are key to reveal a full population of CO clouds in the low-metallicity environment. One of the notable characteristics is the low peak brightness temperature of less than 1 K. This feature is applicable to not only the compact CO clouds but also most of the other clouds in the present observed field (see Figure 3(a)). Suppose the CO emission is optically thick, which is basically applicable to the Galactic molecular clouds; a small beam filling factor results in the observed temperature being well below 10–20 K, the typical temperature of molecular clouds. In other words, the CO clouds are not fully resolved yet even with ~ 2 pc resolution (see the discussion in NGC 6822 by Schruba et al. 2017), and thus the derived column density and density are lower limits.

Figure 6 shows the enlarged views and spectra toward three compact CO clouds. The selection is based on comparing the YSO candidates and the $8 \mu\text{m}$ point source catalog, which is mainly obtained by the Spitzer survey (Gordon et al. 2011; Sewilo et al. 2013). The spatial extension is similar to the beam size, and the peak brightness temperature is 1–2 K, indicating that these clouds are not spatially resolved, as discussed in this section. Although a forthcoming paper (Ohno et al. submitted) provides a further detailed comparison between the infrared sources and the CO properties, we highlight three examples in Figure 6 and discuss what they are.

The left panels show one of the sources associated with a YSO candidate (Sewilo et al. 2013). This particular YSO (Y698) candidate is one of the Stage I sources with a luminosity of $\sim 3 \times 10^3 L_{\odot}$ and a protostellar mass of $\sim 10 M_{\odot}$. The

Table 2. Summary of median physical properties of the compact CO clouds in the SMC North region

Number	T_{peak} [K]	σ_v [km s ⁻¹]	$L_{\text{CO}(2-1)}$ [K km s ⁻¹ pc ²]	R_{deconv} [pc]	N_{H_2} [10 ²¹ cm ⁻²]	M_{CO} [M_{\odot}]	n_{H_2} [10 ² cm ⁻³]	total M_{CO} [10 ⁵ M_{\odot}]
(1)	(2)	(3)	(4)	(5)	(6)	(7)	(8)	(9)
153	1.3	0.52	11.7	1.30	1.1	167	7	0.7

(1) Total number of the identified clouds (2) Peak brightness temperature (3) Velocity dispersion (4) Integrated CO(2–1) luminosity (5) Beam deconvolved radius, $R_{\text{deconv}} = \sqrt{R_{\text{obs}}^2 - R_{\text{beam}}^2}$, where R_{obs} is the geometric mean of the effective rms sizes in major and minor axes multiplied by a factor of 1.91 as suggested by Solomon et al. (1987) and R_{beam} is the beam size in pc (6) Peak H₂ column density with the assumptions of $X_{\text{CO}}^{\text{SMC}} = 6 \times 10^{20} \text{ cm}^{-2} (\text{K km s}^{-1})^{-1}$ and $R_{2-1/1-0} = 0.9$ (see the text in Sect. 4.1) (7) Gas mass with the same assumptions of column 6 (8) Average H₂ volume density, $3M_{\text{CO}}/4\pi\mu m_{\text{H}}R_{\text{deconv}}^3$ where μ is the molecular weight per hydrogen (2.7) and m_{H} is the H atom mass (9) Cumulative M_{CO} in the observed clouds

YSO position fairly corresponds to the CO peak, indicating that the YSO is in an early evolutionary stage of high-mass star formation without destroying the parental cloud. In the LMC, Harada et al. (2019) discovered similar compact CO clouds, which are more than ~ 200 pc apart from nearby GMCs, associated with massive YSO candidates. They also explained that at least one of their targets harbors a stellar cluster instead of a single O-type star. Combining our new findings in the SMC, we demonstrated that such star-forming compact CO clouds do exist in both of the Magellanic Clouds. Some theoretical studies suggest that gas accretion of CO dark H₂ envelope or atomic hydrogen are not negligible as mass supply onto protostars in metal-poor conditions (Krumholz 2012; Fukushima et al. 2020). Additional high-resolution molecular line and H I studies are helpful to advance our understanding of the detailed gas accretion process onto the protostars.

We confirmed that the CO peak and the Spitzer 8 μm source (see the catalog in Gordon et al. 2011) has a good spatial correspondence in the middle panel sources (Figure 6 (c,d)). Although Sewilo et al. (2013) did not catalog this source as a YSO candidate, the good correlation between the source position and molecular gas indicates that the infrared source is not physically unrelated objects, such as external galaxies and evolved stars. Further infrared wavelength analysis is needed to characterize the properties of the central Spitzer source. The right panels show one of the sources without any infrared sources observed by the Spitzer, indicating that the star formation activity is quiescent compared to the other two sources. We cannot prove the CO clouds are purely in a starless phase down to solar and sub-star mass stars. Nevertheless, these infrared-free sources in the SMC may be vital targets to investigate the initial condition of star formation in the metal-poor galaxy.

4.2.2. Enlarged View toward the N66 region and comparison with the MW Orion molecular clouds

Figure 7 presents the comparison between the CO intense cloud, the N66 region, whose moment 0 and peak temperature are the highest in this survey (see Figures 2 and 3(a)), and the Orion molecular clouds in the MW at the same linear scale. The displayed area in panel (a) is located in/around the H II region N66, the largest and most luminous one in the SMC, and hosts nearly 33 OB stars (Massey et al. 1989; Walborn et al. 2000; Evans et al. 2006). The Orion clouds are one of the reasonable targets to show the gas distribution as the typical and well-studied high-mass star-forming region in the MW, although its star formation activity (e.g., Hillenbrand 1997) is not extreme compared to N66. We supplement the ACA map with an alternative ALMA CO($J = 1-0$) data of the N66 region obtained by the ALMA 12 m array (Neelamkudan et al. 2021) to show the higher resolution view. Note that we confirmed the 12 m array data has no significant missing flux based on the comparison between the single-dish SEST spectrum (Rubio et al. 1996) and a smoothed ALMA data at the same angular resolution of 43''.

The N66 region does not show remarkable extended emission in CO, whose size is more than a few tens of parsecs, as seen in Orion. The higher resolution 12 m data shows elongated structures. The spatial extent of CO in N66 is similar to those of C¹⁸O in Orion. Although additional work is required to precisely estimate the actual density traced by the CO observations, CO in the SMC may preferentially trace the innermost part of molecular clouds, whose density is similar to that traced by the C¹⁸O observation in the MW (e.g., Onishi et al. 1996). In fact, ALMA observations by Muraoka et al. (2017) reported that the CO observations in the SMC-N83 region trace $\sim 10^4 \text{ cm}^{-3}$ density gas based on their non-LTE (local thermodynamical equilibrium) analysis using multi-line CO/¹³CO data (see also a lower resolution study by Requena-Torres et al. 2016 in N66). This nature is consistent with the numerical prediction

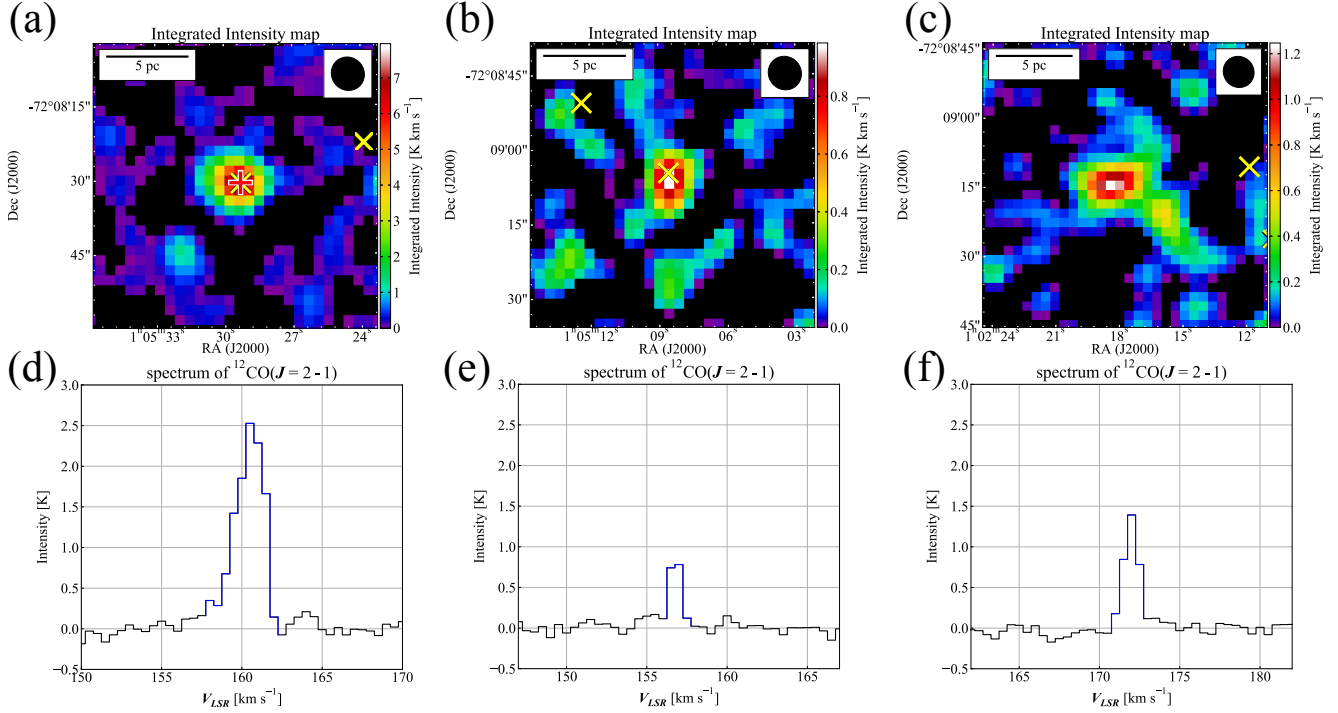


Figure 6. Enlarged-views and their spectra of three of the compact CO clouds (see also the locations as indicated in the white squares in Figure 2(b)). (a) The CO($J = 2-1$) integrated intensity (moment 0) map toward one of the compact CO clouds with the YSO candidate. The emission was integrated over the velocity range from 158.0 to 162.0 km s^{-1} (shown in blue in panel (d)). The beam size of the ACA CO observations is shown in the black ellipse of the upper-right corner. The red and yellow crosses are the high-reliability YSO candidate (Y698) (Sewilo et al. 2013) and $8\mu\text{m}$ sources from the SAGE-SMC catalog (Gordon et al. 2011), respectively. (b,c) Same as (a) but for the cloud associated with and without $8\mu\text{m}$ point source, respectively. The integrated velocity ranges are 156.5–157.5 km s^{-1} for panel (b) and 171.0–172.5 km s^{-1} for panel (c). (d) The CO($J = 2-1$) spectrum extracted from a single-pixel corresponding to the CO peak on panel (a). The highlighted velocity range, 158.0–162.0 km s^{-1} in blue-color, is the significant emission above 3σ noise level. (e,f) Same as (d) but for the sources in panel (b,c), respectively.

that CO dramatically becomes abundant more than an H_2 volume density of $\sim 10^4 \text{ cm}^{-3}$ (Glover & Mac Low 2011; Glover & Clark 2012).

4.2.3. Column density estimation based on the CO and thermal dust emission

Based on the multi-wavelength Herschel PACS/SPIRE data, Jameson et al. (2016) estimated column density distributions of molecular hydrogen in the SMC (hereafter, dust N_{H_2}) at a spatial resolution of $\sim 10 \text{ pc}$ by subtracting the contribution of atomic (H I) gas. Figure 8(a) overlays the CO contours at the native spatial resolution of $\sim 2 \text{ pc}$ on the dust N_{H_2} map. The column density at the compact CO cloud positions ranges $\sim (1-10) \times 10^{20} \text{ cm}^{-2}$. Their CO integrated intensity at $\sim 2 \text{ pc}$ resolution is typically $\sim 1 \text{ K km s}^{-1}$, corresponding to H_2 column density of $\sim 6 \times 10^{20} \text{ cm}^{-2}$ (see the assumptions in Sect. 4.1). This comparison indicates that high-density compact CO clouds are locally embedded at the diffuse H_2 molecular clouds that are not necessarily traced by CO emission.

We tentatively derive the total amount of CO-dark molecular clouds by comparing our CO-based mass and the dust emission. Figure 8(a) shows the dust N_{H_2} map derived by Jameson et al. (2016), which appears to be more widely spread than the CO contours. To compare the two different maps more quantitatively, we spatially smoothed the CO-based N_{H_2} map to be the same spatial resolution ($\sim 10 \text{ pc}$) as the dust N_{H_2} map and then made the ratio map between the two independent measurements (Figure 8(b)). Although we see the ratio of ~ 1 at some CO strong spots, most of the observed field does not exceed the value of 0.2. We derived total H_2 mass as $\sim 6_{-3}^{+6} \times 10^6 M_{\odot}$ within the ACA observed field using the dust-based N_{H_2} map (see Jameson et al. (2016) regarding the description of the factor

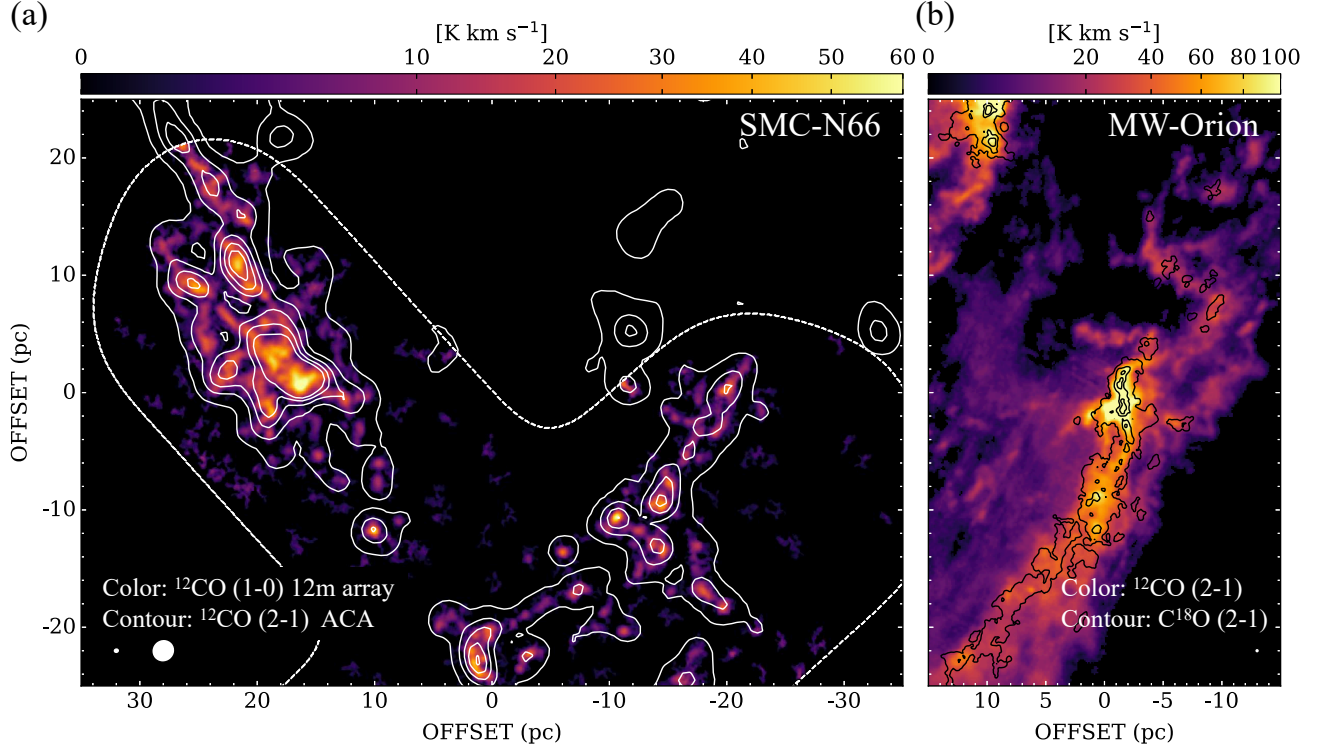


Figure 7. CO distributions of the SMC-N66 region and the Orion molecular cloud in the MW at the same linear scale. (a) The color-scale and contours show the velocity-integrated intensity of CO($J=1-0$) (Neelamkodan et al. 2021) and CO($J=2-1$), respectively. The dotted lines denote the observed region in CO($J=1-0$). The lowest CO($J=2-1$) contour level and contour step are 1 K km s^{-1} and 4 K km s^{-1} , respectively. The small and large ellipses at the lower left corner are the beam sizes of CO($J=2-1$) ACA and CO($J=1-0$) 12 m array data, respectively. (b) The color-scale and contours show the velocity-integrated intensity of CO($J=2-1$) and C 18 O($J=2-1$), respectively (Nishimura et al. 2015) obtained with the Osaka 1.85 m telescope (Onishi et al. 2013). The lowest C 18 O($J=2-1$) contour level and contour step are 1 K km s^{-1} and 3 K km s^{-1} , respectively.

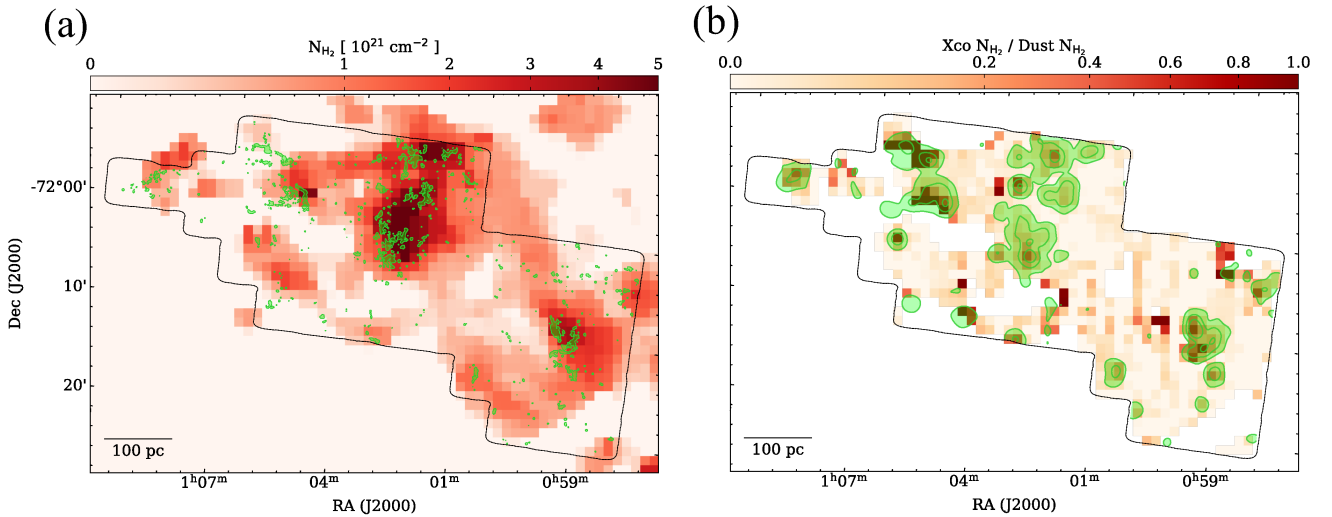


Figure 8. (a) The color-scale image shows the H $_2$ column density map (Jameson et al. 2016). The green contours show the moment 0 map of $^{12}\text{CO}(J=2-1)$ with the lowest contour level of 0.5 K km s^{-1} . (b) The ratio map of H $_2$ column densities derived from X_{CO} based analysis and that in panel (a) (see the text in Sect. 4.2). The green contours are the same as in panel (a) but for spatially smoothed data with a beam size of $1'$ with the contour levels of $[0.05, 0.5, 1.5] \text{ K km s}^{-1}$.

of two uncertainty). The total CO-based molecular mass is $\sim 4 \times 10^5 M_\odot$, and thus we cannot see more than $\sim 90\%$ molecular material in CO, at least in this observed field. This value is significantly higher than the MW observation, $\sim 30\%$ (Grenier et al. 2005), and modeling/numerical studies to mimic MW-like conditions (Wolfire et al. 2010; Smith et al. 2014). Note that there is a caveat in this simple estimation of CO-dark H_2 gas because some studies in the MW suggest that the presence of dark gas is alternatively explained as optically thick cold H I gas (e.g., Fukui et al. 2015b; Hayashi et al. 2019). Higher dust N_{H_2} regions without any CO detection (Figure 8) may represent that the H I emission is saturated due to a high opacity and the analysis failed to fully subtract the atomic gas contribution from the total hydrogen column density. On the other hand, Jameson et al. (2019) reported that there is not a significant component of optically thick H I gas based on their absorption measurements toward 37 out of a total of 55 detected background continuum sources. In this case, the large spatial discrepancy between the dust N_{H_2} and ACA CO maps may be likely due to the lower resolution H I data, $\sim 90''$, than the Herschel-based dust data, $\sim 50''$. Although it is beyond this paper's scope to coordinate the controversial results (c.f., Murray et al. 2018), the detailed analysis using other wavelength data such as H I and gamma-ray emission are desired to understand further the large gap between the CO and dust emission in the SMC.

5. SUMMARY

We presented the CO($J = 2-1$) survey in the SMC North region obtained by the ACA stand-alone mode. The field coverage and the beam size are 0.26 degree^2 ($\sim 2.9 \times 10^5 \text{ pc}^2$) and $6''$ ($\sim 2 \text{ pc}$), respectively. The survey qualities and our early analysis can be summarized as follows:

1. The detection limit in CO luminosity ($L_{CO(2-1)}$) is $\sim 1.0 \text{ K km s}^{-1} \text{ pc}^2$, corresponding to the mass detection threshold of $\sim 10-20 M_\odot$ with assumptions of $\alpha_{CO} = 13 M_\odot (\text{K km s}^{-1} \text{ pc}^2)^{-1}$ and $R_{2-1/1-0} = 0.9$. This sensitivity is two orders of magnitude higher than that of the previous complete CO survey in the SMC (Mizuno et al. 2001).
2. The previously known CO clouds are resolved into spatially-isolated clustered clumps rather than single giant molecular clouds. The sensitive survey detects new faint CO emission (the compact CO clouds) at the positions down to lower H_2 column density ($\sim 10^{20} \text{ cm}^{-2}$) region, judging from the Herschel measurement at ten pc resolution. The observed clouds have a typical peak brightness temperature of $\lesssim 1 \text{ K}$. The possible interpretation is that we cannot fully resolve them even with the $\sim 2 \text{ pc}$ resolution data. It is likely that the beam dilution effect reduces the observed temperature.
3. We investigated some of the compact CO clouds and found infrared point sources, including YSO candidates, associations. The good spatial correspondence to cloud peaks indicates that (high-mass) star formation is ongoing with an early phase before their parental clouds' dissipation. Follow-up studies using higher-resolution molecular line data and more diffuse gas tracers are necessary to unveil the nature of the star-forming compact clouds and accretion process onto the inside protostars.
4. At least within the observed field in the SMC, one of the notable characteristics is that more than 90% of the molecular material is not traced by CO, which is significantly higher than that of the MW study.

ACKNOWLEDGMENTS

We would like to thank the referee, Dr. Katherine E. Jameson for useful comments that improved the manuscript. This paper makes use of the following ALMA data: ADS/ JAO. ALMA#2017.A.00054.S, and #2015.1.01296.S. ALMA is a partnership of ESO (representing its member states), NSF (USA) and NINS (Japan), together with NRC (Canada), MOST and ASIAA (Taiwan), and KASI (Republic of Korea), in cooperation with the Republic of Chile. The Joint ALMA Observatory is operated by ESO, AUI/NRAO, and NAOJ. This work was supported by NAOJ ALMA Scientific Research grant Nos. 2016-03B and Grants-in-Aid for Scientific Research (KAKENHI) of Japan Society for the Promotion of Science (JSPS; grant Nos. JP18K13582, JP18H05440, and JP21H00049). T.W. acknowledges support from NSF grant AST-2009849. We thank Dr. Kei E.I. Tanaka and Dr. Thomas G. Bisbas for discussions on the CO cloud properties and line ratio from theoretical aspects.

Software: CASA (v5.4.0; McMullin et al. 2007), Astropy (Astropy Collaboration et al. 2018), APLpy (Robitaille & Bressert 2012)

APPENDIX

We provide CO($J = 2-1$) and CO($J = 1-0$) data cube and 2-D continuum images in the FITS format as online materials². This Appendix presents the data quality/continuum maps and the intensity ratio of the CO lines.

A. BAND 6/3 DATA: NOISE/CONTINUUM MAPS AND FLUX COMPARISON BETWEEN THE CO(2-1) 7M AND TP ARRAY DATA

Figures 9 and 10 show the r.m.s. noise level of the CO data and 1.3/2.6 mm continuum maps. The noise levels are somewhat depending on region to region, 0.02–0.07 K for CO($J = 2-1$) and 0.2–0.35 K for CO($J = 1-0$), due to different observing conditions in each sub-map.

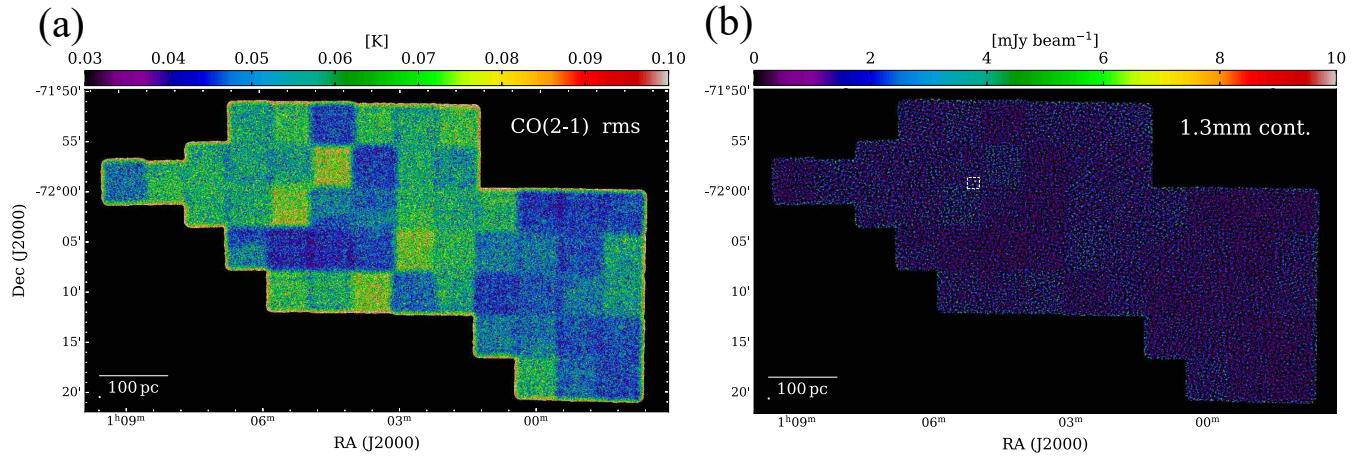


Figure 9. (a) The noise level map of CO($J = 2-1$) data in Band6. (b) The 1.3 mm continuum map. The white rectangle shows the displayed region in Figure 5 (b,c).

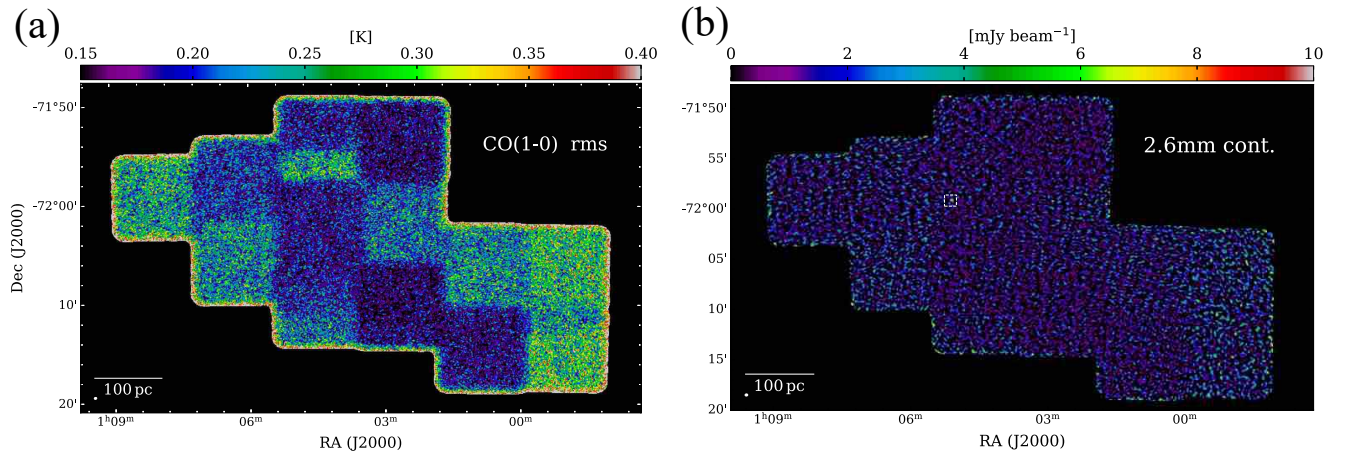


Figure 10. Same as Figure 9 but for Band 3.

Figure 11 shows the TP array and spatially smoothed ACA 7 m array data images in CO(2-1). We coordinated the angular resolutions of both data as 30'', and then, we made the intensity ratio map (panel (b)). The spatially

² <https://doi.org/10.5281/zenodo.4628967>

smoothed 7 m array data well reproduce the TP array distributions, and the mean flux ratio is ~ 0.7 , indicating that more than half of the total CO flux is recovered by the 7 m array alone.

B. CO($J = 1-0$) MAP AND LINE RATIO

Figure 12(a) illustrates the CO($J = 1-0$) distribution in peak brightness temperature, T_{peak} . Due to the poor sensitivity and the beam dilution effect, most of the compact features in CO($J = 2-1$), whose size is close to the Band 6 beam element with the intensity of ~ 1 K, are not detected in CO($J = 1-0$). Since this project did not include TP array observations, we cannot precisely estimate the 7 m array data's missing flux. The spatially smoothed 7 m array data with a beam size of $2.6''$ reproduces the overall CO distribution revealed by the NANTEN survey (Mizuno et al. 2001). Muller et al. (2010) observed several regions in the SMC North region with the single-dish Mopra telescope whose beam size is $\sim 42''$. The CO intensities of the 7 m array corresponds to those with Mopra (see Table 2 in Muller et al. 2010) within the measurement error at least in the available CO intense spots. These comparisons tell us that the missing flux of the 7 m array CO($J = 1-0$) data is not serious.

To discuss the overall intensity ratio of the two transitions ($J = 2-1$ and $1-0$), $R_{2-1/1-0}$, we spatially smoothed both CO data into the beam size of $\sim 30''$. We determined the integrated velocity range based on the higher sensitivity $2-1$ data, and then we applied the same velocity range to make the CO($J = 1-0$) moment 0 map. Figure 12(b) and Figure 13 show the integrated intensity ratio map and the correlation plot, respectively. Note that the current analysis does not contain outer layers of the CO clouds due to the poor sensitivity of the $1-0$ emission. The least-square fitting tells us that the slope is 1.1. Since the CO($J = 1-0$) presumably underestimate the flux due to the interferometric effect (but it is not very large), we adapt $R_{2-1/1-0}$ ratio of 0.9 as a conservative way to estimate the CO luminosity-based mass (see Sect. 4.2).

REFERENCES

- Alaghband-Zadeh, S., Chapman, S. C., Swinbank, A. M., et al. 2013, MNRAS, 435, 1493
- Astropy Collaboration, Price-Whelan, A. M., Sipőcz, B. M., et al. 2018, AJ, 156, 123
- Badenes, C., Maoz, D., & Draine, B. T. 2010, MNRAS, 407, 1301
- Bisbas, T. G., Tan, J. C., & Tanaka, K. E. I. 2021, MNRAS, 502, 2701
- Bolatto, A. D., Leroy, A., Israel, F. P., et al. 2003, ApJ, 595, 167
- Bolatto, A. D., Leroy, A. K., Jameson, K., et al. 2011, ApJ, 741, 12
- Bolatto, A. D., Simon, J. D., Stanimirović, S., et al. 2007, ApJ, 655, 212
- Bolatto, A. D., Wolfire, M., & Leroy, A. K. 2013, ARA&A, 51, 207
- Bot, C., Rubio, M., Boulanger, F., et al. 2010, A&A, 524, A52
- Brunetti, N., Wilson, C. D., Sliwa, K., et al. 2021, MNRAS, 500, 4730
- Corbelli, E., Braine, J., Bandiera, R., et al. 2017, A&A, 601, A146
- Dame, T. M., Hartmann, D., & Thaddeus, P. 2001, ApJ, 547, 792
- Dame, T. M. 2011, arXiv:1101.1499
- de Grijs, R., Wicker, J. E., & Bono, G. 2014, AJ, 147, 122
- Evans, C. J., Lennon, D. J., Smartt, S. J., et al. 2006, A&A, 456, 623
- Fukui, Y., Kawamura, A., Minamidani, T., et al. 2008, ApJS, 178, 56
- Fukui, Y. & Kawamura, A. 2010, ARA&A, 48, 547
- Fukui, Y., Harada, R., Tokuda, K., et al. 2015a, ApJ, 807, L4
- Fukui, Y., Torii, K., Onishi, T., et al. 2015b, ApJ, 798, 6
- Fukui, Y., Tokuda, K., Saigo, K., et al. 2019, ApJ, 886, 14
- Fukushima, H., Yajima, H., Sugimura, K., et al. 2020, MNRAS, 497, 3830
- Glover, S. C. O. & Mac Low, M.-M. 2011, MNRAS, 412, 337
- Glover, S. C. O. & Clark, P. C. 2012, MNRAS, 426, 377
- Glover, S. C. O. & Clark, P. C. 2016, MNRAS, 456, 3596
- Gordon, K. D., Meixner, M., Meade, M. R., et al. 2011, AJ, 142, 102
- Gordon, K. D., Roman-Duval, J., Bot, C., et al. 2014, ApJ, 797, 85
- Graczyk, D., Pietrzyński, G., Thompson, I. B., et al. 2020, ApJ, 904, 13
- Grenier, I. A., Casandjian, J.-M., & Terrier, R. 2005, Science, 307, 1292
- Harada, R., Onishi, T., Tokuda, K., et al. 2019, PASJ, 71, 44
- Hayashi, K., Mizuno, T., Fukui, Y., et al. 2019, ApJ, 884, 130

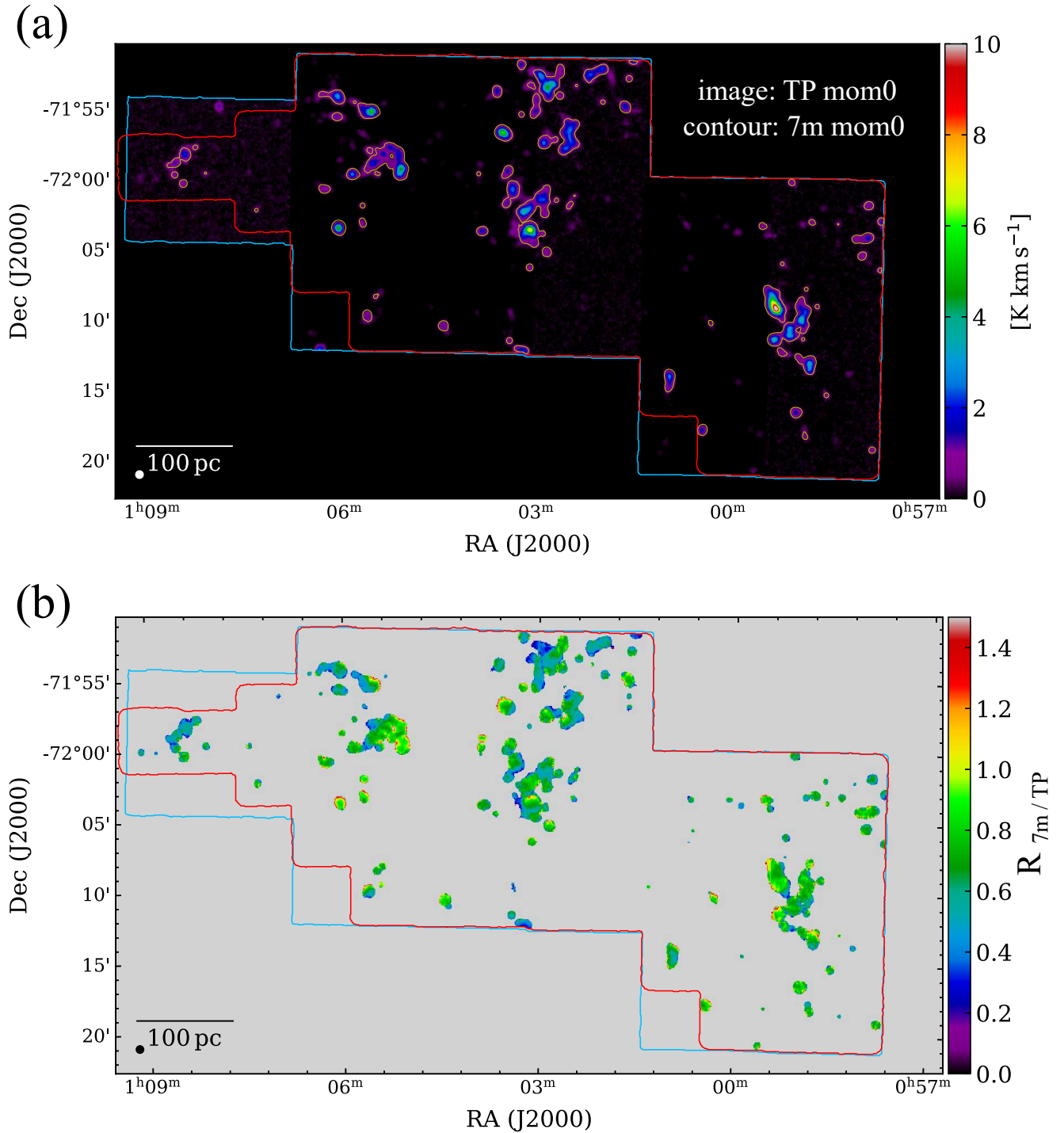


Figure 11. (a) The color-scale image illustrates the TP moment 0 map in CO(2–1). Yellow contours show the smoothed moment 0 map obtained with the 7 m with a contour level of 0.3 K km s^{-1} . The white circle at the lower left corner is the TP array beam size, $30''$. The red and blue lines show the field coverage of 7 m and TP, respectively. (b) The color-scale image shows distributions of the ACA 7 m/TP CO($J = 2-1$) integrated intensity ratio. We ignored a low level emission less than 0.06 K , which corresponds to 3σ level of the TP array data. The integrated velocity range is $114.5-232.0 \text{ km s}^{-1}$. The black circle at the lower left corner is the TP array beam size, $30''$.

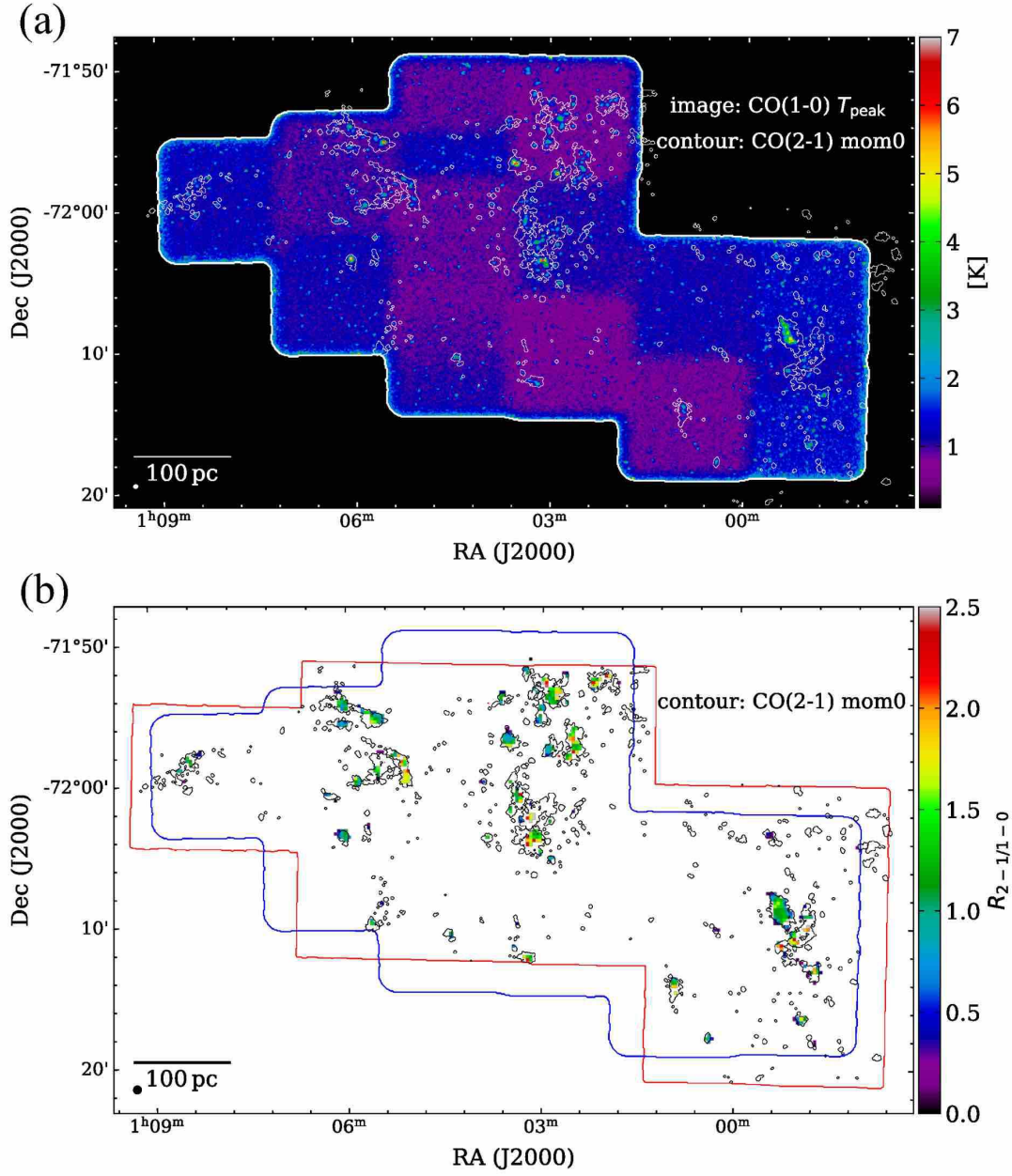


Figure 12. (a) The color-scale image illustrates the CO($J=1-0$) T_{peak} map. The beam size is given by the white ellipse in the lower-left corner. White contours show the moment 0 map of CO($J=2-1$) with the contour level of 1 K km s^{-1} . (b) Integrated intensity ratio, CO($J=2-1$)/CO($J=1-0$) ($R_{2-1/1-0}$) map (see the text). The smoothed beam size ($30''$) is shown in the lower-left corner. Black contours are the same as the white ones in panel (b). The red and blue lines show the field coverage of CO($J=2-1$) and CO($J=1-0$), respectively.

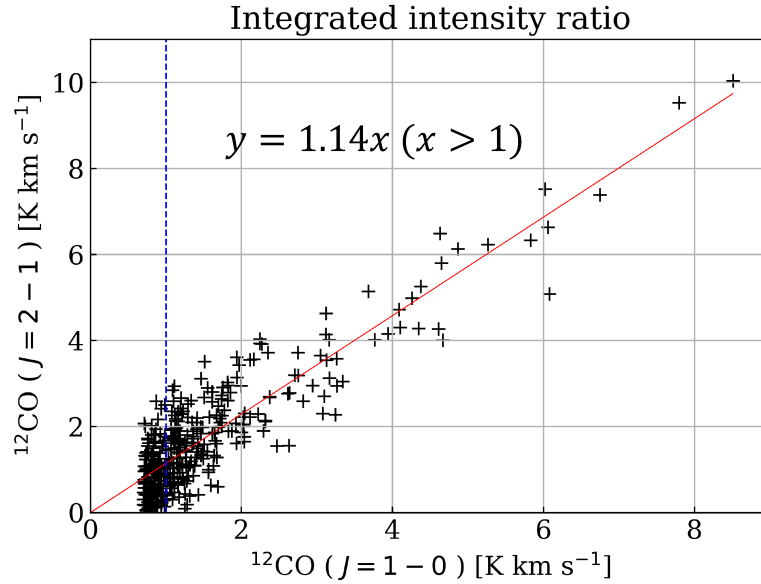


Figure 13. The correlation plot between the integrated intensity of CO($J=2-1$) and CO($J=1-0$) at an angular resolution of $30''$. The red line shows the fitting result obtained by the least-square method. The weak emission less than 1 K km s^{-1} (shown in the blue dotted line) were not used in the fitting.

- Henize, K. G. 1956, *ApJS*, 2, 315
- Hillenbrand, L. A. 1997, *AJ*, 113, 1733
- Hony, S., Gouliermis, D. A., Galliano, F., et al. 2015, *MNRAS*, 448, 1847
- Indebetouw, R., Brogan, C., Chen, C.-H. R., et al. 2013, *ApJ*, 774, 73
- Jameson, K. E., Bolatto, A. D., Leroy, A. K., et al. 2016, *ApJ*, 825, 12
- Jameson, K. E., Bolatto, A. D., Wolfire, M., et al. 2018, *ApJ*, 853, 111
- Jameson, K. E., McClure-Griffiths, N. M., Liu, B., et al. 2019, *ApJS*, 244, 7
- Kepley, A. A., Tsutsumi, T., Brogan, C. L., et al. 2020, *PASP*, 132, 024505
- Kondo, H., Tokuda, K., Muraoka, K., et al. 2021, *ApJ*, 912, 66
- Krumholz, M. R. 2012, *ApJ*, 759, 9
- Maggi, P., Filipović, M. D., Vukotić, B., et al. 2019, *A&A*, 631, A127
- Massey, P., Parker, J. W., & Garmany, C. D. 1989, *AJ*, 98, 1305
- McClure-Griffiths, N. M., Dénes, H., Dickey, J. M., et al. 2018, *Nature Astronomy*, 2, 901
- McMullin, J. P., Waters, B., Schiebel, D., et al. 2007, *Astronomical Data Analysis Software and Systems XVI*, 127
- Miura, R. E., Kohno, K., Tosaki, T., et al. 2012, *ApJ*, 761, 37
- Mizuno, N., Rubio, M., Mizuno, A., et al. 2001, *PASJ*, 53, L45
- Murray, C. E., Peek, J. E. G., Di Teodoro, E. M., et al. 2019, *ApJ*, 887, 267
- Murray, C. E., Peek, J. E. G., Lee, M.-Y., et al. 2018, *ApJ*, 862, 131
- Muller, E., Ott, J., Hughes, A., et al. 2010, *ApJ*, 712, 1248
- Muraoka, K., Homma, A., Onishi, T., et al. 2017, *ApJ*, 844, 98
- Muraoka, K., Kondo, H., Tokuda, K., et al. 2020, *ApJ*, 903, 94
- Naslim, N., Tokuda, K., Onishi, T., et al. 2018, *ApJ*, 853, 175
- Neelamkodan, N., Tokuda, K., Barman, S., et al. 2021, *ApJL*, 908, L43
- Nazé, Y., Hartwell, J. M., Stevens, I. R., et al. 2002, *ApJ*, 580, 225
- Nishimura, A., Tokuda, K., Kimura, K., et al. 2015, *ApJS*, 216, 18
- Okada, Y., Requena-Torres, M. A., Güsten, R., et al. 2015, *A&A*, 580, A54
- Okada, Y., Güsten, R., Requena-Torres, M. A., et al. 2019, *A&A*, 621, A62
- Oliveira, J. M., van Loon, J. T., Sloan, G. C., et al. 2013, *MNRAS*, 428, 3001
- Onishi, T., Mizuno, A., Kawamura, A., et al. 1996, *ApJ*, 465, 815
- Onishi, T., Nishimura, A., Ota, Y., et al. 2013, *PASJ*, 65, 78

- Onodera, S., Kuno, N., Tosaki, T., et al. 2010, *ApJL*, 722, L127
- Onodera, S., Kuno, N., Tosaki, T., et al. 2012, *PASJ*, 64, 133
- Ossenkopf, V. & Henning, T. 1994, *A&A*, 291, 943
- Pagel, B. E. J. 2003, *CNO in the Universe*, 304, 187
- Papadopoulos, P. P., Thi, W.-F., & Viti, S. 2004, *MNRAS*, 351, 147
- Pei, Y. C., Fall, S. M., & Hauser, M. G. 1999, *ApJ*, 522, 604
- Pety, J., Schinnerer, E., Leroy, A. K., et al. 2013, *ApJ*, 779, 43
- Requena-Torres, M. A., Israel, F. P., Okada, Y., et al. 2016, *A&A*, 589, A28
- Robitaille, T., & Bressert, E. 2012, *APLpy: Astronomical Plotting Library in Python*, ascl:1208.017
- Rolleston, W. R. J., Dufton, P. L., McErlean, N. D., et al. 1999, *A&A*, 348, 728
- Rolleston, W. R. J., Trundle, C., & Dufton, P. L. 2002, *A&A*, 396, 53
- Roman-Duval, J., Gordon, K. D., Meixner, M., et al. 2014, *ApJ*, 797, 86
- Rosolowsky, E. W., Pineda, J. E., Kauffmann, J., et al. 2008, *ApJ*, 679, 1338
- Rubio, M., Garay, G., Montani, J., et al. 1991, *ApJ*, 368, 173
- Rubio, M., Lequeux, J., Boulanger, F., et al. 1993, *A&A*, 271, 1
- Rubio, M., Lequeux, J., Boulanger, F., et al. 1996, *A&AS*, 118, 263
- Ruffle, P. M. E., Kemper, F., Jones, O. C., et al. 2015, *MNRAS*, 451, 3504
- Russell, S. C. & Dopita, M. A. 1992, *ApJ*, 384, 508
- Saigo, K., Onishi, T., Nayak, O., et al. 2017, *ApJ*, 835, 108
- Sakamoto, S., Hayashi, M., Hasegawa, T., et al. 1994, *ApJ*, 425, 641
- Sano, H., Tsuge, K., Tokuda, K., et al. 2021, *PASJ*, 73, S62
- Sawada, T., Koda, J., & Hasegawa, T. 2018, *ApJ*, 867, 166
- Schinnerer, E., Meidt, S. E., Pety, J., et al. 2013, *ApJ*, 779, 42
- Schruba, A., Leroy, A. K., Kruijssen, J. M. D., et al. 2017, *ApJ*, 835, 278
- Sewilo, M., Carlson, L. R., Seale, J. P., et al. 2013, *ApJ*, 778, 15
- Smith, R. C., & MCELS Team 1999, *New Views of the Magellanic Clouds*, 190, 28
- Smith, R. J., Glover, S. C. O., Clark, P. C., et al. 2014, *MNRAS*, 441, 1628
- Solomon, P. M., Rivolo, A. R., Barrett, J., et al. 1987, *ApJ*, 319, 730
- Stanimirovic, S., Staveley-Smith, L., Dickey, J. M., et al. 1999, *MNRAS*, 302, 417
- Sun, J., Leroy, A. K., Schruba, A., et al. 2018, *ApJ*, 860, 172
- Takekoshi, T., Minamidani, T., Komugi, S., et al. 2017, *ApJ*, 835, 55
- Takekoshi, T., Minamidani, T., Komugi, S., et al. 2018, *ApJ*, 867, 117
- Tokuda, K., Fukui, Y., Harada, R., et al. 2019, *ApJ*, 886, 15
- Tokuda, K., Muraoka, K., Kondo, H., et al. 2020a, *ApJ*, 896, 36
- Tokuda, K., Fujishiro, K., Tachihara, K., et al. 2020b, *ApJ*, 899, 10
- Tosaki, T., Kuno, N., Onodera, S. M., et al. 2011, *PASJ*, 63, 1171
- Walborn, N. R., Lennon, D. J., Heap, S. R., et al. 2000, *PASP*, 112, 1243
- Wolfire, M. G., Hollenbach, D., & McKee, C. F. 2010, *ApJ*, 716, 1191
- Wong, T., Hughes, A., Tokuda, K., et al. 2017, *ApJ*, 850, 139
- Wong, T., Hughes, A., Tokuda, K., et al. 2019, *ApJ*, 885, 50
- Yajima, Y., Sorai, K., Miyamoto, Y., et al. 2021, *PASJ*, 73, 257
- Ye, T., Turtle, A. J., & Kennicutt, R. C. 1991, *MNRAS*, 249, 722
- Yoda, T., Handa, T., Kohno, K., et al. 2010, *PASJ*, 62, 1277